Spatial distribution of neutral oxygen vacancies on ZnO nanowire surfaces: An investigation combining confocal microscopy and first principles calculations

Kin Mun Wong, S. M. Alay-e-Abbas, Yaoguo Fang, A. Shaukat, and Yong Lei

Articles you may be interested in

First principles investigations on the electronic structure of anchor groups on ZnO nanowires and surfaces
J. Appl. Phys. **115**, 203720 (2014); 10.1063/1.4879676

Interaction of light with the ZnO surface: Photon induced oxygen "breathing," oxygen vacancies, persistent photoconductivity, and persistent photovoltage
J. Appl. Phys. **115**, 033701 (2014); 10.1063/1.4861413

First-principles investigation of the size-dependent structural stability and electronic properties of O-vacancies at the ZnO polar and non-polar surfaces
J. Appl. Phys. **113**, 014304 (2013); 10.1063/1.4772647

Size effects on formation energies and electronic structures of oxygen and zinc vacancies in ZnO nanowires: A first-principles study
J. Appl. Phys. **109**, 044306 (2011); 10.1063/1.3549131

Mechanistic investigation of ZnO nanowire growth
Appl. Phys. Lett. **95**, 183114 (2009); 10.1063/1.3258074

Spatial distribution of neutral oxygen vacancies on ZnO nanowire surfaces: An investigation combining confocal microscopy and first principles calculations

Kin Mun Wong,[1,a)] S. M. Alay-e-Abbas,[2,3] Yaoguo Fang,[1] A. Shaukat,[3] and Yong Lei[1,b)]

[1]*Institut für Physik & IMN MacroNano® (ZIK), Technische Universität Ilmenau, Prof. Schmidt-Str. 26, Ilmenau 98693, Germany*
[2]*Department of Physics, GC University Faisalabad, Allama Iqbal Road, Faisalabad 38000, Pakistan*
[3]*Department of Physics, University of Sargodha, 40100 Sargodha, Pakistan*

A qualitative approach using room-temperature confocal microscopy is employed to investigate the spatial distribution of shallow and deep oxygen vacancy (V_O) concentrations on the polar (0001) and non-polar ($10\bar{1}0$) surfaces of zinc oxide (ZnO) nanowires (NWs). Using the spectral intensity variation of the confocal photoluminescence of the green emission at different spatial locations on the surface, the V_O concentrations of an individual ZnO NW can be obtained. The green emission at different spatial locations on the ZnO NW polar (0001) and non-polar ($10\bar{1}0$) surfaces is found to have maximum intensity near the NW edges, decreasing to a minimum near the NW center. First-principles calculations using simple supercell-slab (SS) models are employed to approximate/model the defects on the ZnO NW ($10\bar{1}0$) and (0001) surfaces. These calculations give increased insight into the physical mechanism behind the green emission spectral intensity and the characteristics of an individual ZnO NW. The highly accurate density functional theory (DFT)-based full-potential linearized augmented plane-wave plus local orbitals (FP-LAPW + lo) method is used to compute the defect formation energy (DFE) of the SSs. Previously, using these SS models, it was demonstrated through the FP-LAPW + lo method that in the presence of oxygen vacancies at the (0001) surface, the phase transformation of the SSs in the graphite-like structure to the wurtzite lattice structure will occur even if the thickness of the graphite-like SSs are equal to or less than 4 atomic graphite-like layers [Wong *et al.*, J. Appl. Phys. **113**, 014304 (2013)]. The spatial profile of the neutral V_O DFEs from the DFT calculations along the ZnO [0001] and [$10\bar{1}0$] directions is found to reasonably explain the spatial profile of the measured confocal luminescence intensity on these surfaces, leading to the conclusion that the green emission spectra of the NWs likely originate from neutral oxygen vacancies. Another significant result is that the variation in the calculated DFE along the ZnO [0001] and [$10\bar{1}0$] directions shows different behaviors owing to the non-polar and polar nature of these SSs. These results are important for tuning and understanding the variations in the optical response of ZnO NW-based devices in different geometric configurations. © *2013 Author(s). All article content, except where otherwise noted, is licensed under a Creative Commons Attribution 3.0 Unported License.* [http://dx.doi.org/10.1063/1.4813517]

I. INTRODUCTION

Zinc oxide (ZnO) nanostructures of different sizes and shapes, such as nanowires (NWs), nanobelts, nanodots, and nanosheets, have been fabricated using various synthesis techniques. Some of these techniques include chemical vapor deposition (CVD),[1] the electrochemical deposition method,[2] using an anodic aluminum oxide template[3,4] as an evaporation mask, sputtering process,[5] plasma-enhanced atomic layer deposition,[6] and sol-gel methods.[7] In addition to being fundamental constituents of functional electronic and electrical devices, ZnO and other semiconductor based nanomaterials have been the subject of much multidisciplinary experimental and theoretical research owing to their immense importance in technological applications such as nanomedicine,[8] optoelectronic devices,[9] and as a heterogeneous catalyst for the production of different chemicals.[10]

It is well known that ZnO nanostructures contain a large density of intrinsic defects such as oxygen deficiencies or vacancies (V_O), which influence their electronic and optical properties as well as their performance in device applications.[11,12] Because the size of the ZnO-based devices can range from a few nanometers to several micrometers and the surface-to-volume ratio can be quite large, the distribution of the nanostructure's shallow intrinsic surface defects and deep intrinsic bulk defects plays a crucial role in tailoring the properties of the device. For example, the study of the spatial distribution of defects on the surfaces and interfaces

a)Author to whom correspondence should be addressed. Electronic addresses: kin-mun.wong@tu-ilmenau.de and km2002wong@yahoo.com.sg
b)Electronic mail: yong.lei@tu-ilmenau.de

114, 034901-1

of nanostructure-based field-effect transistors is important for understanding its electronic properties.[13,14] In particular, the performance of nano-optoelectronic devices using ZnO-based 1D nanostructures is strongly dependent upon the concentration and distribution of the V_O in the ZnO nanostructures, and the conductivity of ZnO NWs was found to correlate with the concentration of V_O and size of the NWs.[15] Also, the electrical performance of ZnO nanowire field effect transistors (NW-FETs) is found to be significantly influenced by oxygen vacancies, which serve as chemisorbed sites for oxygen molecules.[11,12] In this way, vacancies create a surface depletion region and band bending that significantly alter the channel conductivity of the NW-FETs.

There is a strong directional dependence of the ZnO NW properties[16] corresponding to several different device configurations. Two common configurations involve a vertical and horizontal array of ZnO NWs along the [0001] and [10$\bar{1}$0] directions. The (0001) and (10$\bar{1}$0) surfaces are also important because they occur predominantly at the surfaces of the synthesized ZnO nanostructures.[17,18] Although the effects of V_O on the optical and electrical properties of bulk and nanoscale ZnO structures have been extensively investigated, the spatial distribution of the V_O concentration in ZnO NW surfaces has not yet been evaluated.

In this paper, we adopt a combined experimental and theoretical study of the spatial electronic profile of the surface and deep V_O in ZnO NWs in the [0001] and [10$\bar{1}$0] directions. Since the luminescence intensity is directly correlated with the V_O concentration, confocal microscopy measurements can provide a non-destructive and direct qualitative measurement of the V_O concentration at the ZnO NWs surfaces.[15,19] Using this approach, we are able to achieve a better qualitative understanding of the spatial distribution of the surface defects in the NW, thus leading to a more efficient functionalization and integration of the ZnO NW-based devices for improved performance. To gain insight into the basic mechanisms that govern the confocal optical properties of the ZnO NWs in the [0001] and [10$\bar{1}$0] directions, we employ density functional theory (DFT) calculations using the full-potential linearized augmented plane-wave plus local orbitals (FP-LAPW + lo) method. We also demonstrate the suitability of supercell-slab (SS) models in the surface simulations as an approximation of the ZnO NW cross sections from where the confocal measurements are taken.

II. EXPERIMENTAL DETAILS AND STRUCTURAL MODELS USED IN THE CALCULATIONS

The morphology of the ZnO NW arrays was characterized with a Nova NanoSEM scanning electron microscope (SEM) 50 series 230 (FEI, USA). The high-resolution transmission electron microscopy (HRTEM) samples were created by dropping a small amount of sample dispersion onto a carbon-coated 300-mesh copper grid and subsequently drying it at room temperature, and HRTEM images were acquired with a JEOL JEM-2010F transmission electron microscope (Japan) at an acceleration voltage of 200 kV. The X-ray diffraction (XRD) patterns were acquired with a

D/MAX-2550 diffractometer (Rigaku, Japan) equipped with a CuKα radiation source ($\lambda = 1.54178$ Å) and a rotating anode. The phonon vibrational characteristics of the ZnO NWs were obtained at room temperature using a backscattering geometry on a Renishaw inVia Raman microscope with a laser excitation of 514 nm. The confocal photoluminescence (CPL) measurements presented in this article were taken at room temperature with a PicoQuant MicroTime 200 confocal microscope, with the ZnO NW sample luminescence excited using a 375 nm-wavelength pulsed diode laser at a constant intensity. The time-correlated single photon counts were acquired using a single photon avalanche diode detector and a PicoHarp 300 from PicoQuant (Berlin, Germany). The photon count data were then analyzed using the PicoQuant SymPhoTime software package (version 5.13).

The ZnO NW arrays were synthesized using a CVD process in a horizontal tube furnace where the Si (100) substrate was initially cleaned with alcohol (99.7% purity) and then with acetone (99.5% purity) in an ultrasonic bath.[15] Subsequently, the cleaned Si substrate was etched in a mixed solution of 20 ml of ammonia hydroxide (25%), 20 ml of hydrogen peroxide (30%), and 100 ml of deionized water at 80 °C. A thin film of ZnO crystal seeds was attained by spin-coating 5–7 layers of an alcoholic solution of zinc acetate dehydrate (2M) on the Si substrate, followed by annealing in an oven at 120 °C for 30 min. Equal amounts of ZnO powder (99.0% purity) and graphite (99.85% purity) at 0.5 g each was mixed and ground together. The ground mixtures were then placed in an alumina boat which was positioned at the center of the furnace tube, and the substrate prepared earlier containing a thin film of ZnO crystal seeds was positioned above the source material. At this point, 2 sccm (standard cubic centimeters per minute) of oxygen gas and 70 sccm of argon gas were introduced into the furnace tube and the pressure in the tube was held at about 200 mbar. Finally, the temperature in the tube was raised to 950 °C at a rate of 25 °C min^{-1} and this temperature was maintained for about 20–25 min, followed by a natural cooling of the furnace tube to room temperature.

To better understand the spatial profile of the ZnO NW luminescence intensity, DFT-based WIEN2K computer code[20] was used to compute the electronic structure of the ZnO SSs in an artificial crystal symmetry. The non-polar (10$\bar{1}$0)/($\bar{1}$010) and polar (0001)/(000$\bar{1}$) surfaces were used in the calculations to approximate the horizontal and vertical cross-sectional areas in the ZnO NWs, as shown in Figs. 1(a) and 1(b). The SSs used to replicate the polar and non-polar surfaces were constructed by stacking the ZnO primitive unit cells along the c-axis and a-axis of the hexagonal lattice, followed by a vacuum region of several Å along these two axes to decouple the interactions between the SSs.[21] Figure 1(a) shows the graphical representation of the horizontal $6 \times 1 \times 1$ (24 atoms) SS that is repeated infinitely along the hexagonal b- and c-axes. Figure 1(b) shows the graphical representation of the vertical $1 \times 1 \times 5$ (20 atoms) SS that is repeated infinitely along the hexagonal a- and b-axes. For further details of the structural models and the stable termination of the $1 \times 1 \times 5$ SS at the basal plane, the reader is referred to Ref. 21.
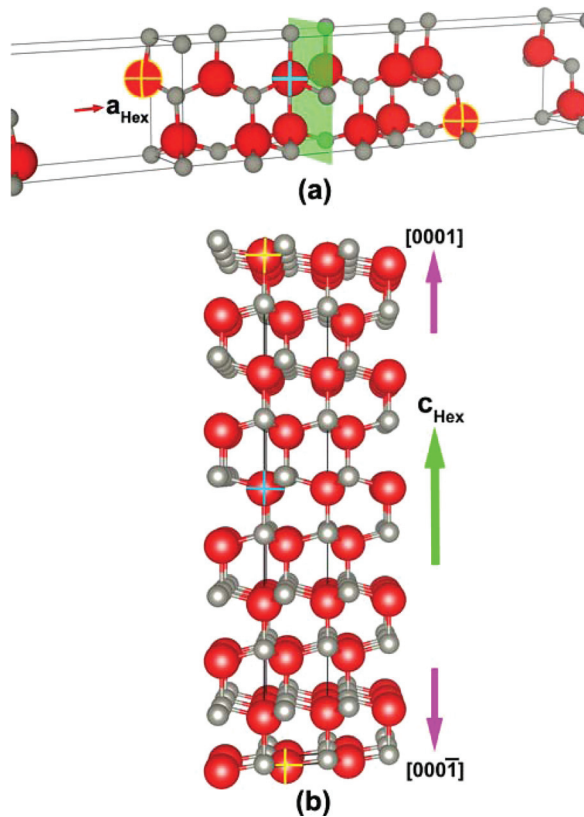
(a)

(b)

FIG. 1. (a) Side view of the $6 \times 1 \times 1$ SS used for approximating the horizontal cross section of the ZnO NW, and the vacuum region used to decouple the interactions between the consecutive SSs. The green plane represents the center of the $6 \times 1 \times 1$ SS. (b) Side view of the $1 \times 1 \times 5$ SS used in the approximation of the vertical cross section of the ZnO NW. The O, Zn, surface O-vacancy, and deep O-vacancy atoms are represented by the large red, small grey, yellow-crossed, and blue-crossed spheres, respectively. The $6 \times 1 \times 1$ and $1 \times 1 \times 5$ SSs are obtained by stacking the ZnO primitive unit cells along the a_{Hex} and c_{Hex} directions, respectively.

In a recent study,[21] we showed that the heat of formation, H_f, obtained within the generalized gradient approximation parameterization scheme of Perdew *et al.*[22] is in good agreement with both experimental and theoretical values for bulk ZnO.[23] Therefore, for the whole set of DFT calculations reported in the current study, the exchange and correlation potential were treated using the PBEsol functional. Previously, using these SS models, it was demonstrated through the FP-LAPW + lo method that in the presence of oxygen vacancies at the (0001) surface, the phase transformation of the SSs in the graphite-like structure to the wurtzite lattice structure will occur even if the thickness of the graphite-like SSs are equal to or less than 4 atomic graphite-like layers [Ref. 21]. For the $1 \times 1 \times 5$ and $6 \times 1 \times 1$ SSs, a Monkhorst-Pack[24] **k**-point mesh of $(18 \times 18 \times 1)$ and $(9 \times 5 \times 1)$, respectively, for the first Brillouin zone integration was used in the calculations, which was found to be sufficient for energy and charge convergence. Self-consistency in the SS calculations was achieved by iterative convergence of the minimum total energy to a value below 0.0001 Ry, and the Hellman-Feynman forces to a value below 1 mRy/a.u. In these calculations, the core electrons were treated fully relativistically, while a scalar relativistic approximation was used for the valence states. The basis function was
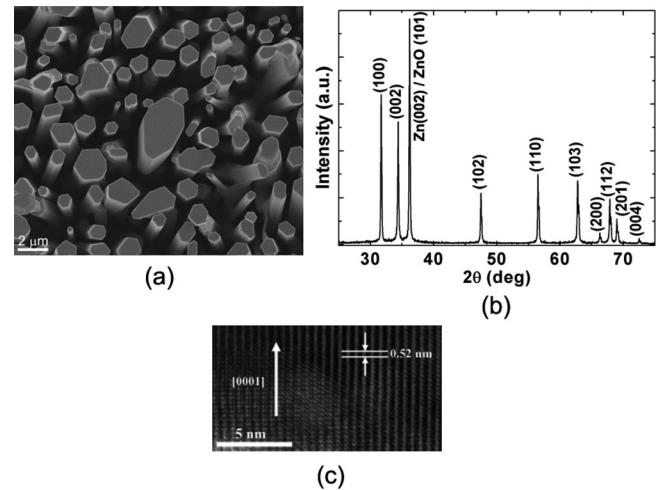
expanded up to $R_O x K_{max} = 7.0$ and the angular expansion up to $l = 10$ in the muffin tins, where $R_O = 0.79$ Å is the muffin-tin radius of the O atom and K_{max} is the maximal reciprocal lattice vector. In the interstitial region, a charge density and potential Fourier plane wave expansion up to $G_{max} = 12$ were used. No spin-orbit (SO) couplings were taken into account in these calculations, because the main objective of SO incorporation is to obtain SO splitting in the band structure,[25,26] and it has a negligible effect upon the total energy calculations required for computing the defect formation energy (DFE).

III. RESULTS AND DISCUSSION

A. Structural characterization of the ZnO NW arrays

The SEM image in Fig. 2(a) shows the morphology of the ZnO NW arrays that are fabricated using the chemical vapor deposition process.[15] As seen in the image, the cross section of most of the ZnO NWs is in the range of 1–2 μm. Crystallographic characterization and quality of the synthesized ZnO NW arrays are measured using XRD and HRTEM. The diffraction peaks in the XRD pattern shown in Fig. 2(b) can be indexed as the hexagonal wurtzite structure of ZnO, the sharpness of the peaks indicating the crystallinity of the synthesized ZnO NWs.[27] All of the peaks found in the XRD spectra can be indexed to hexagonal ZnO with a wurtzite structure (JCPDS Card Nos. 36–1451 and 89–7102), and characteristic peaks belonging to other chemical compounds are not observed. We acknowledge that the XRD peak at $2\theta = 36.2°$ can be assigned to the (002) plane of pure Zn, though in this case the XRD peak intensity might be due to a mixture of the reflections from the (101) plane of ZnO and the (002) plane of Zn. However, experimental work on the hierarchical structure of ZnO nanorods showing the comparison between the magnitude of the (101) diffraction peak of ZnO with that of the (002) diffraction peak of Zn clearly shows that the intensity of the Zn (002) diffraction peak is much weaker than that of the ZnO (101) diffraction peak.[28] Therefore, even if the XRD peak at $2\theta = 36.2°$ consists of a mixture of the

(a)

(b)

(c)

FIG. 2. (a) Typical top view SEM image showing the cross section and (b) an XRD pattern of the ZnO NW arrays. (c) An HRTEM image of a single ZnO NW.

reflections from the ZnO (101) plane and the Zn (002) plane, the pure Zn in the NWs would not significantly affect their photoluminescence. It is, however, beyond the scope of this paper to examine the full details of the effects of pure Zn on the photoluminescence of the ZnO NWs, though work of this nature can be carried out in the future.

Besides the 10 XRD peaks shown in Fig. 2(b), the magnitude of the other diffraction peaks in the data is insignificant and could reasonably be attributed to noise. Therefore, even if the additional small peaks could be indexed to pure Zn, their effect on the CPL measurements would be negligible. The strong (100) diffraction peak can be indexed to the hexagonal ($10\bar{1}0$) crystal surfaces predominantly present in ZnO NWs. On the other hand, the lattice seen in the HRTEM image in Fig. 2(c) has a measured spacing of 0.52 nm, which corresponds well with the distance between two (0001) planes of wurtzite ZnO. This is evidence that the ZnO NW arrays grow along the [0001] direction.

Raman spectra have been successfully used to identify the crystal orientation of wurtzite ZnO NWs.[29] ZnO belongs to the $C_{6\nu}$ symmetry group, and from group theory prediction the optical modes at the Γ point of the Brillion zone are given by $\Gamma = A_1 + 2B_1 + E_1 + 2E_2$.[16] The A_1 and E_1 modes represent the vibration of atoms parallel and perpendicular to the hexagonal c-axis, respectively, they are both infrared and Raman-active, and they are each further divided into longitudinal optical (LO) and transverse optical (TO) components. The Raman peak at 331 cm^{-1} is assigned to the A_1(acoustic overtone).[29] The low and high frequencies of the E_2 mode (E_2(low), E_2(high)) are exclusively Raman-active and correspond to the vibration of the Zn and O sublattice, respectively.[16] The B_1 modes, however, are silent and inactive. Importantly, it was experimentally observed that the presence of both the A_1(acoustic overtone) and A_1(TO) bands centered at 331 and 380 cm^{-1}, respectively, is associated with the orientation of the ZnO nanostructure perpendicular to the c-axis, while the absence of both of these modes is associated with the orientation of the ZnO nanostructure parallel to the c-axis.[29] Observing the Raman spectra of our synthesized ZnO NWs, shown in Fig. 3, the negligible signal of both the A_1(acoustic overtone) and A_1(TO) bands from our samples indicates that our ZnO NWs are oriented
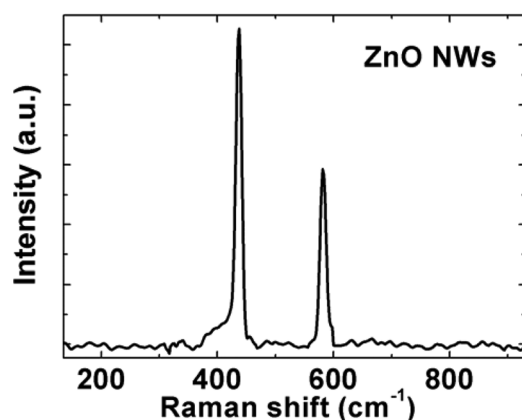

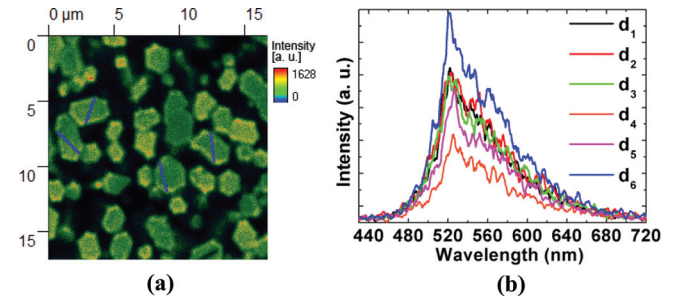FIG. 3. Raman spectrum of the ZnO NW arrays.

FIG. 4. (a) Spatially resolved CPL intensity microscope image of the ZnO NW arrays. The blue lines represent locations where the CPL spectra are taken at different spatial locations. (b) Plot of several CPL spectra of the green luminescence taken at different spatial locations along the blue guide line across the cross section surface of one laterally elongated ZnO NW.

preferentially along the c-axis. This is in agreement with the TEM image in Fig. 2(c), which confirms the ZnO NW growth along the c-axis. Raman spectra are also sensitive to structural defects in the synthesized ZnO NWs, and the presence of the E_1(LO) peak at around 582 cm^{-1} is associated with V_O defects.[30]

B. Confocal photoluminescence of the ZnO NW arrays at the (0001) and ($10\bar{1}0$) surface

Figure 4(a) shows the scanned images which map the CPL emission intensity from the ZnO NW arrays obtained using a PicoQuant MicroTime 200 confocal microscope. These images are obtained by scanning an area of $16.8 \times 17.1 \, \mu m$. From the outline of the cross section of the NWs seen in the figure, most of the ZnO NWs are hexagonal-shaped with a diameter of 1–2 μm along with a few laterally elongated NWs with cross-sectional sizes larger than 2 μm. This is quite similar to the NW shapes and sizes observed in the SEM image in Fig. 2(a). The spatially resolved CPL emission intensity of the ZnO NW arrays is inhomogeneously distributed. This could be due to the difference in the NW heights, where the NWs with a distinct emission intensity outline are in the focal plane and the NWs with weaker emission intensity are longer or shorter. This could be the case because, in confocal microscopy, light emitted above or below the focal plane is not efficiently collected. It is worth pointing out that for the (0001) surface of one NW, the variation of the CPL intensity at the surface is not significantly affected by the presence of other NWs in its vicinity. Also, the SEM image shown Fig. 2(a) shows that the (0001) surface of the NW is relatively flat, and changes in the maxima of the CPL spectra at different spatial locations along the blue line (drawn only as a guide for eye) in Fig. 4(a) are therefore most likely due to variation in the spatial distribution of surface atoms and defects.

The unambiguous assignment of green luminescence to a particular defect is difficult because of the varying conditions and/or synthesis methods under which ZnO nanostructures are fabricated. In the literature, for example, a number of origins have been proposed for the green PL emission bands centered at 510 nm. Some studies attribute it to impurities such as copper.[31] Other proposed physical mechanisms behind the green visible luminescence are point defects such

as oxygen vacancies (V_O),[32,33] zinc vacancies (V_{Zn}),[34] zinc interstitials (Zn_i),[35] and antisite oxygen (O_{Zn}).[36] The energy-dispersive X-ray spectra of our NW arrays taken after the CVD growth reveal only the presence of Zn and O elements (data not shown). This confirms that the synthesized NW arrays are primarily ZnO and do not contain any other impurities at the surface or within the volume of the NWs. Apart from the two common defect types of V_O and V_{Zn}, which have low DFEs,[37] other intrinsic defects such as Zn_i are unstable at room temperature.[38] On the other hand, native defects such as O_{Zn} and defect complexes (combination of native defects) have a high formation energy and are therefore not typically present in large concentrations under normal conditions.[37,39,40]

For the NW arrays in this work, synthesized using the CVD process, it is observed that the green emission band peak remains at almost the same position ($\lambda \approx 519$ nm) for NWs synthesized with different oxidation temperatures and durations. This is in agreement with earlier experimental work by Vanheusden *et al.*, which shows that the peak of the green luminescence band that holds nearly the same position at different oxidation temperatures correlates well with V_O defects.[19,41,42] In other experimental observations, the concentration of V_{Zn} defects decreases at higher temperatures.[43,44] The NW arrays in this work, as shown in Fig. 2(a), were synthesized using the CVD process at a high temperature of 950 °C. Therefore, from these multiple arguments, we believe that V_O defects are responsible for the green luminescence emitted by our synthesized NW arrays, as obtained using CPL microscopy measurements. The magnitude of the measured CPL spectra can therefore also be correlated to the concentration of the oxygen vacancies in the ZnO NWs.

Since the confocal volume at the spot where the excitation laser beam hits is the "well-defined" volume within a sample that the confocal microscopy system detects, it is important to calculate the lateral and axial resolution of the confocal volume in the x-y and z planes. The lateral and axial resolution in the x-y and z planes (as defined using the Rayleigh criterion), respectively, is given by[45]

$$LR_{xy} = \frac{0.61\lambda_{ex}}{NA}, \tag{1}$$

$$AR_z = \frac{1.5n\lambda}{NA^2}, \tag{2}$$

where λ_{ex} is the excitation wavelength, NA is the numerical aperture of the objective, and n is the index of refraction of the mounting media. For our CPL measurements, $\lambda_{ex} = 375$ nm, $NA = 1.48$ from the manufacturer, and $n = 1.5$ for the oil used.

From Eq. (1), the lateral dimension resolution of the confocal microscope (i.e., lateral spot size) at the top cross-sectional area of the ZnO NW surface is about 155 nm. It is therefore justifiable to select an average spacing between measurements of about 400 nm. This distance of about 2.5 times the lateral spot size between the centers of two adjacent lateral spot sizes (the spot where the excitation laser

beam hits) minimizes the overlap and interference of the measurements at these two spatial locations. To obtain the spatial distribution of the oxygen vacancies, V_O, in the (0001) planes of the synthesized ZnO NWs, four different laterally elongated ZnO NWs are selected. On each of these four ZnO NWs, CPL spectra are acquired at six different spatial locations arranged along a straight path, indicated by the blue guide line in Fig. 4(a), in the top cross-sectional (0001) plane of the NWs. Each CPL spectrum is the measurement of the luminescence emitted from the spot where the excitation laser beam hits. The larger and laterally elongated NWs are selected because they have the necessary physical dimensions for proper spatial resolution of the confocal intensity across the top of the ZnO (0001) surface.

To ease quantifying the spatial variation of the spectral intensity along each of the four blue lines as plotted in Fig. 4(b), the midpoint between the center of the two innermost spots where the excitation laser beam hits is taken as the origin ($d = 0$ μm). The spatial distances of the center of each of the six lateral spots, d_x (where x = 1, 2, 3, 4, 5, and 6), are calculated from this origin point. For example, the distances from the origin of the center of the two innermost locations where the excitation laser beam hits are indicated as d_3 and d_4. The variation in the green PL peak of the CPL spectra corresponding to the six spatial locations along the guide line for one of the ZnO NW (0001) surfaces will be discussed later, along with DFE calculations. It is worth pointing out that there are slight variations in the peak values at d_x (where x = 1, 2, 3, 4, 5, and 6) for each of the four different NWs because the origin point for each line is located at a different spot on the (0001) plane.

In Fig. 4(b), each CPL spectrum plotted is obtained at different spatial locations on the top (0001) surface of a ZnO NW. The magnitude of the green luminescence peak in each individual CPL spectra at a particular location on the (0001) surface of the ZnO NW can be correlated with the concentration and the DFE of V_O at that particular spatial location, which we will explain in detail in the next section. Furthermore, the shape and peak position of each green luminescence peak at each spatial location remain essentially the same ($\lambda \approx 519$ nm), which reinforces the viewpoint that the magnitude of each CPL peak at $\lambda \approx 519$ nm can be used as a measure of the amount of oxygen vacancies at that particular spatial location. The overall CPL spectra are a function of different spatial locations on the top (0001) surface of the ZnO NW and, in other words, are dependent upon the different spatial locations from which the emission occurred. However, the magnitude of each individual CPL spectra shown in Fig. 4(b) is a function of the emission from a specific spatial location and, because ZnO luminescence is very sensitive to the surface state of ZnO,[15,19] the green PL peak at $\lambda \approx 519$ nm can therefore be correlated to the amount of V_O at that spatial location.

Earlier in this section we showed that the underlying mechanism of the green PL emission in ZnO nanostructures is likely due to oxygen vacancies.[19,41,42] It is commonly hypothesized that the green PL peak at about 519 nm (≈ 2.39 eV) originates from singly ionized oxygen vacancies (V_o^+) due to the recombination of the V_o^+ electron with the

photoexcited holes in the valence band.[19] Some uncertainties about this hypothesis remain, however, because of doubts about the definite assignment of the electron paramagnetic resonance signal at g = 1.46 to the transition between the V_o^+ defect and the photoexcited hole.[46] It is also well known from first principle calculations[40] that the V_o^+ defects are unstable, so the oxygen vacancies will be either in the neutral state (V_O) or the doubly charged state (V_o^{++}), depending upon the Fermi level position. In some recently proposed luminescence mechanisms for ZnO nanostructures, it is generally agreed that owing to surface defects that act as gas adsorption sites, the upward band bending at the surface results in a surface depletion region at the boundaries of the NWs.[47,48] In addition, at room temperature the V_o^+ and V_o^{++} centers can only exist in the surface depletion layer owing to the ionization of V_O, and the nanostructure interior holds neutral V_O.[47,48] Owing to the carriers generated from thermal activation and laser illumination during the confocal measurements, the depth of the surface recombination layer at the (0001) surface and at the vertical edges of the NWs (where the (0001) surface and the side walls meet each other) is usually less than 60 nm.[47,48] Using Eq. (2), we can quantify the axial resolution of the confocal measurements and find the confocal volume wherein the atoms are being probed. For our microscope, the confocal volume can extend several hundreds of nanometers below the top ZnO (0001) surface. Because d_1 and d_6 are located at least hundreds of nanometers away from the vertical edges of the NWs, the green PL emission from our micro-sized ZnO NWs at different spatial locations (as seen in Fig. 4(b)) is therefore likely to be from the neutral V_O.

Figure 5(a) shows the CPL emission intensity of an individual thin ZnO NW lying on a side composed of the (10$\bar{1}$0) surface. The spatial location of the center of the three spots where the measurements were taken, l_x (where x = 1, 2, 3), is calculated in relation to the slanted top edge where the (0001) and (10$\bar{1}$0) surface meet each other (located near the upper right corner of the NW in the figure). The CPL spectra taken at these three positions are along a path parallel to the wurtzite c-axis. This corresponds to a vertical cross section of the (10$\bar{1}$0) surface along the [0001] growth direction of the NW that is lying on its side, as shown in Fig. 5(a). Figure 5(b) shows the green CPL spectra acquired at the three

different spatial locations (l_1, l_2, and l_3), where it can be seen that the shape and location of the peaks remain approximately unchanged and only the peak intensity of the CPL spectra changes, decreasing in the [000$\bar{1}$] direction along the vertical cross section of the NW. Similar CPL measurements were repeated on three different ZnO NWs lying on their (10$\bar{1}$0) surfaces.

C. Comparison of V_O defect formation energies with the CPL spectra at the (0001) and (10$\bar{1}$0) surface

We discussed in the previous section that the underlying mechanism of the green CPL emission is likely due to the neutral V_O, which is capable of green emission owing to direct and indirect emission processes.[49] We have also concluded from Eq. (2) that the confocal volume wherein the atoms are being probed via CPL measurements can extend several hundreds of nanometers below the surface, where the effect of surface band bending is absent and the ionization of V_O is negligible. Therefore, only the DFE of the neutral V_O is considered in our calculations. The DFE of the neutral V_O is calculated using[21]

$$E(V_o) = E_t^d - E_t^p - \Sigma \Delta n_o \mu_o + q E_F, \qquad (3)$$

where E_t^d, E_t^p, E_F, and q are the minimum total energies of the O-deficient ZnO SS, the perfect ZnO SS, the Fermi energy level, and the charge state of the defect, respectively; Δn_o is the difference in the number of O atoms between the perfect and defective SS and μ_o is the chemical potential of oxygen under O-rich and O-poor conditions.

The SSs used in this study are not large enough to imitate the horizontal (along the [$\bar{1}$010] direction) and vertical (along the [0001] direction) cross sections of a micron-sized NW. Nevertheless, the trends in the structural and electronic properties calculated from a SS consisting of a few ZnO

(a)

(b)   **(c)**

FIG. 6. (a) Schematic diagram of a single ZnO NW showing the top (0001) surface and side walls of the NW. (b) and (c) Enlarged confocal intensity images showing the six spatial locations where the CPL measurements are taken on an individual NW at the (0001) surface. Each rectangular dotted box in the figure represents a single $N \times 1 \times 1$ SS model.

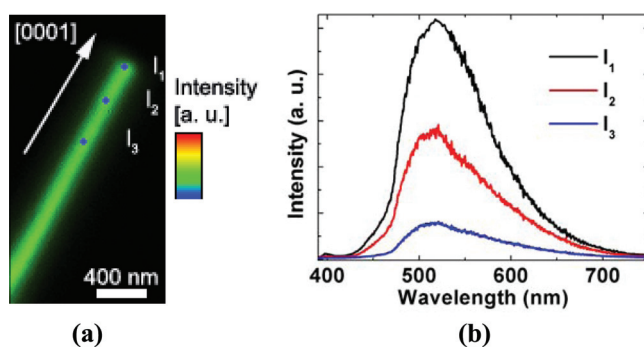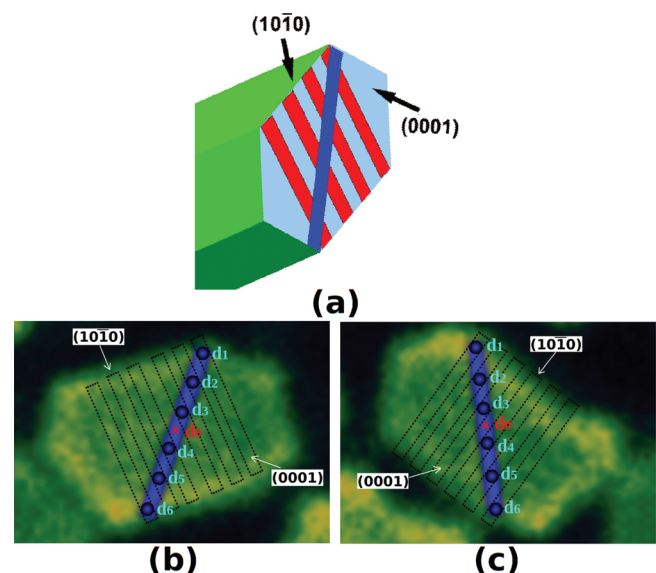**(a)**   **(b)**

FIG. 5. (a) CPL intensity microscope image of a thin ZnO NW lying on its side. (b) The CPL spectra at three different spatial locations along the [0001] direction, which corresponds to a vertical cross-section of the NW that is lying on its side.

wurtzite unit cells can be extrapolated to the cross section of an actual NW. To illustrate this point, a schematic diagram of the top section of a ZnO NW is presented in Fig. 6(a). The light blue surface at the top of the NW is the Zn-terminated (0001) surface, while the six side faces of the NW in green (three visible in front and three hidden by the NW in the background) correspond to the mixed-terminated ZnO surfaces composed of $(10\bar{1}0)$ surfaces. For a comparative analysis of the composition and orientations of various wurtzite ZnO surfaces, the reader is referred to Ref. 50. In Fig. 6(a), the blue rectangle at the Zn-terminated (0001) surface of the schematic wurtzite ZnO NW represents the horizontal cross section along which the confocal measurements in Fig. 4(a) are taken.

It should be noted that Fig. 6(a) is a slanted representation of the Zn-terminated (0001) surfaces of a ZnO NW, as compared with the surfaces shown in Fig. 4(a) and Figs. 6(b) and 6(c) with blue guide lines across their faces. Since the six side walls of the schematic NW, as shown in Fig. 6(a), correspond to mixed-terminated ZnO surfaces, each red rectangular box orthogonal to the [0001] direction should correspond to an $N \times 1 \times 1$-type SS that is terminated along the hexagonal a-axis and is infinite along the hexagonal b- and c-axes. The red rectangular box in Fig. 6(a) and the dotted rectangular boxes in Figs. 6(b) and 6(c) all represent an $N \times 1 \times 1$ SS, but the small number of red rectangular boxes in Fig. 6(a) and the dotted rectangular boxes in Figs. 6(b) and 6(c) are for illustration purposes only. In a real NW, there may be many such $N \times 1 \times 1$ SSs stacked side by side and having a large value of N, much larger than the $N = 6$ considered for simulation in this work.

Looking at the blue rectangle depicted in Fig. 6(a) that goes from one side wall of the NW to the other (starting and ending at the mixed-terminated ZnO surfaces), it is clear that a point randomly chosen on the blue rectangle should belong to one of the $N \times 1 \times 1$ SSs stacked adjacent and parallel to each other. This can be seen more clearly by looking at the intersections between the blue rectangle and the red rectangles as shown in Fig. 6(a). For clarification, blue lines and dotted rectangles are overlaid on images of the (0001) surface of two of the most uniform NWs [taken from Fig. 4(a)] and are shown in Figs. 6(b) and 6(c). These NW images are

enlarged and give a schematic representation of the six CPL measurements as a function of distance from the origin and their correspondence with the simulation results. As has already been discussed for Fig. 6(a), if we consider that each dotted rectangle shown in Figs. 6(b) and 6(c) is a single $N \times 1 \times 1$ SS, the mixed-terminated ZnO $(10\bar{1}0)$ surface of the SS is found at the shorter edge of the rectangle.

The six blue spheres along the blue line in Figs. 6(b) and 6(c) represent the confocal volumes of the CPL measurements taken along the horizontal cross-section of the NW and belong to different horizontal $N \times 1 \times 1$ SSs spanning the width of the NW. These spheres are designated as d_1 through d_6, and are referenced with respect to the red cross, d_0, which represents the origin. Again, we stress that the schematic representation of $N \times 1 \times 1$ SSs should not be considered as an actual representation because the micron-sized NWs shown in Figs. 6(b) and 6(c) would consist of hundreds or even thousands of such SSs. The length of each $N \times 1 \times 1$ SS is a collection of unit cells stacked along the cross-sectional direction of the ZnO NW, the hexagonal a-axis in Fig. 1(a), that starts and terminates at the mixed-terminated ZnO $(10\bar{1}0)$ and $(\bar{1}010)$ surfaces. The justification that the $N \times 1 \times 1$ SS with mixed-terminated ZnO surfaces can represent the side walls of our NWs can be based on two facts: (a) the DFE value, V_O, of the O atom located in the interior of the SS is close to the bulk V_O value (described in more detail below); and (b) the spatial profile of the calculated V_O DFE values along the hexagonal a-axis (with $N = 6$) agrees with the spatial profile of the peak magnitude of the CPL measurements presented in Fig. 7(b). Hence, a $N \times 1 \times 1$ SS with $N = 6$ is a good choice for reliable theoretical results and also enables a reasonable computational time for the first-principles calculations.

Because the confocal volume of the CPL measurements is at least several nanometers away from the probed (0001) ZnO surface, the CPL measurement is taken in a semi-bulk-like environment. Furthermore, each measured CPL point along the cross section of the ZnO NW always belongs to at least one wurtzite unit cell. Our $N \times 1 \times 1$ SSs are simply a collection of these unit cells stacked along the cross-sectional direction from the $(10\bar{1}0)$ plane to the $(\bar{1}010)$, so the CPL measurements are comparable to the DFE values
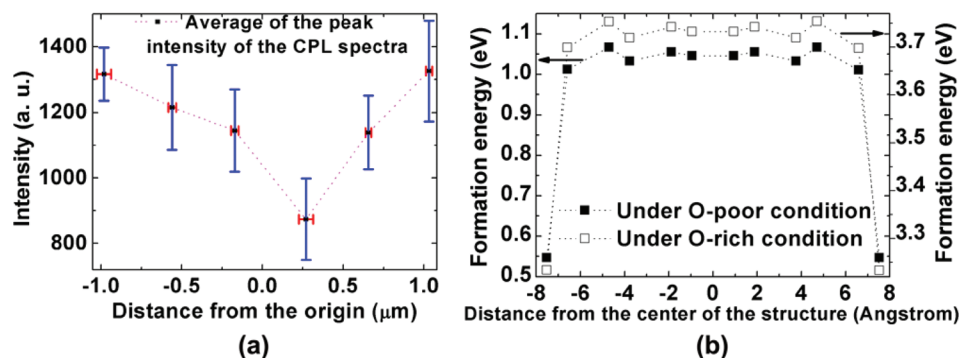

FIG. 7. (a) Variation of the average maximum intensity of the green emission CPL spectra at the locations d_1, d_2, d_3, d_4, d_5, and d_6 over the horizontal cross-sectional surface of four different laterally elongated ZnO NWs. (b) The O defect formation energies at different spatial locations along the $6 \times 1 \times 1$ SS calculated using the Wien2k simulation program (under both O-rich and O-poor conditions). The spatial locations are calculated with respect to the center of the structure.
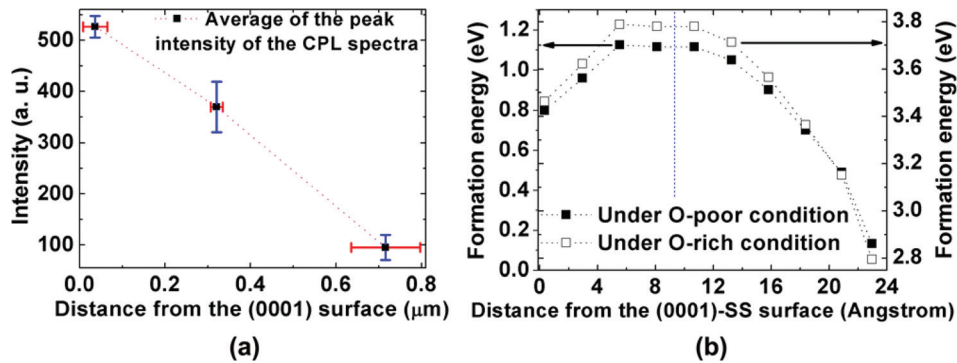
FIG. 8. (a) Variation of the average maximum intensity of the CPL spectra at the locations l_1, l_2, and l_3 over the vertical cross-sectional $(10\bar{1}0)$ surface of four different ZnO NWs lying on their sides. (b) The O defect formation energies at different spatial locations along the $1 \times 1 \times 5$ SS calculated under both O-rich and O-poor conditions. The spatial locations on the NW lying on its side are calculated with respect to the slanted top edge where the (0001) and $(10\bar{1}0)$ surface meet each other.

computed theoretically for a $6 \times 1 \times 1$ SS that extends infinitely along the hexagonal b- and c-axes.

Figure 7(a) is a statistical plot showing the average maximum intensity of the CPL spectra for each d_x of four different ZnO NWs. The d_x (where x = 1, 2, 3, 4, 5, and 6) location values correspond to the four different ZnO NWs (blue lines) as shown in Fig. 4(b), and the vertical error bars indicate the ± 1 standard error of the CPL spectral intensity measurement. It is quite apparent that the maximum intensities of the CPL spectra measured furthest away from the origin (d_1 and d_6) are higher than those closest to the origin (d_3 and d_4). This trend can be explained in terms of the oxygen DFE at different spatial locations along the $6 \times 1 \times 1$ SS under both O-rich and O-poor conditions, whose calculated values are shown in Fig. 7(b). We can see in Fig. 7(b) that the calculated formation energies at the edges of the SS are much lower than those in the interior of the $6 \times 1 \times 1$ SS, which is consistent with the bulk limit of the V_O DFE reported in earlier studies.[51] This implies that the O vacancy defect density and the corresponding maximum CPL spectra intensity of the green emission should be higher near the NW vertical edges where the (0001) surface and the $(10\bar{1}0)$ side walls meet each other, which is what we observe experimentally in Fig. 4(b). From the formation energy values shown in Fig. 7(b), it is evident that a simple planar $(10\bar{1}0)$ SS surface could replicate the experimentally observed spatial characteristics of the CPL spectra and thereby provide a reasonable model of the ZnO NW cross sections where the experimental confocal measurements were taken.

Figure 8(a) shows the statistical plot of the average maximum intensity of the CPL spectra for four different NWs. The different spatial locations, designated as l_1, l_2, and l_3, are taken along the vertical [0001] growth direction near the top end of the NW below the ZnO NW $(10\bar{1}0)$ surface and are referenced with respect to the slanted top edge where the (0001) and $(10\bar{1}0)$ surfaces meet each other. The error bars indicate the ± 1 standard error of the intensity. The magnitude of the average maximum intensity of the CPL spectra significantly decreases almost linearly across the NW, the value decreasing from the edge towards the middle of the NW. This is in reasonable agreement with the linear increase of the first three calculated DFE values (i.e., between 0 and

6 Å) presented in Fig. 8(b), with the first value calculated at $l_1 \approx 0$ Å at the top (0001)-SS surface and progressing towards the interior of the $1 \times 1 \times 5$ SS. To help clarify the discussion that follows, it will be beneficial to review Figs. 1(a) and 1(b) and the graphical representations given of the $6 \times 1 \times 1$ SS and $1 \times 1 \times 5$ SS. We will adopt the same argument that was used earlier for the horizontal cross section of the ZnO NW to interpret the spatial profile of the calculated V_O DFE values that increase while moving toward the center of the $1 \times 1 \times N$-type SS. This increase in the DFE suggests a reduced V_O concentration in the interior of the SS compared with the (0001)-SS surface, which corresponds well with the decrease of the CPL luminescence intensity observed in Fig. 8(a). Looking at Figs. 7 and 8, the calculated DFE trends in the non-polar and polar SSs can satisfactorily explain the observed spatial CPL profile along the $[10\bar{1}0]$ direction and the $[0001]$ direction, respectively. When comparing the calculated DFE data for the whole length of the $1 \times 1 \times 5$ SS [Fig. 8(b)] with the corresponding CPL spectra data, it is important to point out that the behavior observed at the $N \times 1 \times 1$ and $1 \times 1 \times N$ SS ends is different because of their non-polar and polar natures, respectively. In the case of the $N \times 1 \times 1$ SS, we showed that the DFE variation of both sides of the SS towards the middle of the SS is the same. However, in the case of the $1 \times 1 \times N$ SS, the variation in the calculated DFE values from the (0001)-SS surface and $(000\bar{1})$-SS surface towards the center should be fundamentally different because these surfaces have opposite polarity. Because the trend in the CPL spectra have shown a direct correlation with the computed DFE values for the case originating at a (0001)-SS surface and moving towards the interior of the $1 \times 1 \times N$ SS, the computed DFE values presented in Fig. 8(b) between 10 Å and 24 Å lead us to make two important predictions regarding the possible trends in the CPL spectra for the case originating at a $(000\bar{1})$ surface and moving to the interior a NW if it were to grow along the [0001] direction with a bare O-terminated surface at the bottom of the NW. First, a much smaller DFE value calculated at the $(000\bar{1})$ surface compared with that at the (0001) surface indicates the possibility of a higher V_O concentration at the O-terminated surface that would incidentally lead to a higher average CPL intensity than the

intensity obtained for l$_1$ as depicted in Fig. 8(a). Second, the rapid increase of the calculated DFE from 24 Å to 18 Å, more rapid than that seen from 0 Å to 6 Å, implies that data originating at the (000$\bar{1}$) surface would see a more prominent decrease in the CPL spectra maximum intensity than the CPL data presented in Fig. 5(b).

From all of the information presented in Figs. 7 and 8, it can be deduced that the CPL spectra are directly related to the density of the neutral oxygen vacancies. This provides unambiguous evidence that the higher intensity of green emission at the NW edges compared with the interior regions is likely caused by the presence of a larger density of neutral O vacancies at the edges.

IV. CONCLUSIONS

In summary, confocal microscopy is used to qualitatively map the spatial profile of the V$_O$ concentration on the (10$\bar{1}$0) and (0001) surfaces of ZnO NWs because the V$_O$ concentration is demonstrated to be directly correlated with the confocal luminescence intensity. The spatial profile of the luminescence intensity indicates that the V$_O$ concentration is largest near the edges of the (0001) and (10$\bar{1}$0) surfaces of the NWs, and likewise, the confocal measurements demonstrate that the V$_O$ concentrations reduce significantly in the interior parts of the NWs. These results are interpreted using first-principles density functional calculations of the DFE by modeling polar and non-polar SSs to investigate the spatial profile of the neutral O-vacancy along these surfaces. The calculations show that the neutral V$_O$ formation energy is lower near the boundary and increases to bulk-like values in the SS center. The calculations also indicate that the SSs provide adequate approximations for modeling the horizontal and vertical cross-sections of the ZnO NWs because we find that the calculated V$_O$ formation energy along the SS is satisfactorily able to explain the observed trend in the confocal luminescence intensity spatial profile. Furthermore, owing to the polar and non-polar natures of $1 \times 1 \times 5$ SS and $6 \times 1 \times 1$ SS, the DFE variations along the respective SSs are different. The results reported in this paper are useful for understanding the optoelectronic properties of the ZnO NW surfaces that are influenced by oxygen defects, thereby enabling improvement in the integration of ZnO NWs in future nanodevices.

[1]D.-S. Kang, S. K. Han, J.-H. Kim, S. M. Yang, J. G. Kim, S.-K. Hong, D. Kim, H. Kim, and J.-H. Song, J. Vac. Sci. Technol. B **27**, 1667 (2009).
[2]D. Pradhan, Z. Su, S. Sindhwani, J. F. Honek, and K. T. Leung, J. Phys. Chem. C **115**, 18149 (2011).
[3]Y. Lei, Z. Jiao, M. H. Wu, and G. Wilde, Adv. Eng. Mater. **9**, 343 (2007).
[4]Y. Lei, C. H. Liang, Y. C. Wu, L. D. Zhang, and Y. Q. Mao, J. Vac. Sci. Technol. B **19**, 1109 (2001).
[5]P. Kumar, H. K. Malik, A. Ghosh, R. Thangavel, and K. Asokan, Appl. Phys. Lett. **102**, 221903 (2013).
[6]C. Zhu, D. J. Smith, and R. J. Nemanich, J. Vac. Sci. Technol. B **30**, 051807 (2012).
[7]G. M. Ali and P. Chakrabarti, J. Vac. Sci. Technol. B **30**, 031206 (2012).
[8]D. A. Groneberg, M. Giersig, T. Welte, and U. Pison, Curr. Drug Targets **7**, 643 (2006).
[9]G. Murtaza and I. Ahmad, J. Appl. Phys. **111**, 123116 (2012).
[10]M. Kurtz, J. Strunk, O. Hinrichsen, M. Muhler, K. Fink, B. Meyer, and C. Wöll, Angew. Chem., Int. Ed. **44**, 2790 (2005).
[11]Z. Fan, D. Wang, P.-C. Chang, W.-Y. Tseng, and J. G. Lu, Appl. Phys. Lett. **85**, 5923 (2004).
[12]W. Wang, H. D. Xiong, M. D. Edelstein, D. Gundlach, J. S. Suehle, C. A. Richter, W.-K. Hong, and T. Lee, J. Appl. Phys. **101**, 044313 (2007).
[13]K. M. Wong, W. K. Chim, K. W. Ang, and Y. C. Yeo, Appl. Phys. Lett. **90**, 153507 (2007).
[14]K. M. Wong and W. K. Chim, Appl. Phys. Lett. **88**, 083510 (2006).
[15]K. M. Wong, Y. Fang, A. Devaux, L. Wen, J. Huang, L. D. Cola, and Y. Lei, Nanoscale **3**, 4830 (2011).
[16]T. N. Duc, K. Singh, M. Meyyappan, and M. M. Oye, Nanotechnology **23**, 194015 (2012).
[17]J. Q. Hu, Y. Bando, J. H. Zhan, Y. B. Li, and T. Sekiguchi, Appl. Phys. Lett. **83**, 4414 (2003).
[18]N. Moloto, S. Mpelane, L. M. Sikhwivhilu, and S. S. Ray, Int. J. Photoenergy **2012**, 189069.
[19]K. Vanheusden, W. L. Warren, C. H. Seager, D. R. Tallant, J. A. Voigt, and B. E. Gnade, J. Appl. Phys. **79**, 7983 (1996).
[20]P. Blaha, K. Schwarz, G. K. H. Madsen, D. Kvasnicka, and J. Luitz, *WIEN2K, An Augmented Plane Wave + Local Orbitals Program for Calculating Crystal Properties* (Karlheinz Schwarz, Techn. Universität Wien, Austria, 2001).
[21]K. M. Wong, S. M. Alay-e-Abbas, A. Shaukat, Y. Fang, and Y. Lei, J. Appl. Phys. **113**, 014304 (2013).
[22]J. P. Perdew, A. Ruzsinszky, G. I. Csonka, O. A. Vydrov, G. E. Scuseria, L. A. Constantin, X. Zhou, and K. Burke, Phys. Rev. Lett. **100**, 136406 (2008).
[23]F. Oba, A. Togo, I. Tanaka, J. Paier, and G. Kresse, Phys. Rev. B **77**, 245202 (2008).
[24]H. J. Monkhorst and J. D. Pack, Phys. Rev. B **13**, 5188 (1976).
[25]P. Carrier and S.-H. Wei, Phys. Rev. B **70**, 035212 (2004).
[26]K. M. Wong, S. M. Alay-e-Abbas, A. Shaukat, and Y. Lei, Solid State Sci. **18**, 24 (2013).
[27]O. Lupan, L. Chow, G. Chai, and H. Heinrich, Chem. Phys. Lett. **465**, 249 (2008).
[28]D. Zhang, X. Wu, N. Han, and Y. Chen, J. Nanopart. Res. **15**, 1580 (2013).
[29]C.-T. Chien, M.-C. Wu, C.-W. Chen, H.-H. Yang, J.-J. Wu, W.-F. Su, C.-S. Lin, and Y.-F. Chen, Appl. Phys. Lett. **92**, 223102 (2008).
[30]Z. Q. Chen, A. Kawasuso, Y. Xu, H. Naramoto, X. L. Yuan, T. Sekiguchi, R. Suzuki, and T. Ohdaira, J. Appl. Phys. **97**, 013528 (2005).
[31]N. Y. Garces, L. Wang, L. Bai, N. C. Giles, L. E. Halliburton, and G. Cantwell, Appl. Phys. Lett. **81**, 622 (2002).
[32]S. A. Studenikin, N. Golego, and M. Cocivera, J. Appl. Phys. **84**, 2287 (1998).
[33]N. E. Hsu, W. K. Hung, and Y. F. Chen, J. Appl. Phys. **96**, 4671 (2004).
[34]Y. W. Heo, D. P. Norton, and S. J. Pearton, J. Appl. Phys. **98**, 073502 (2005).
[35]M. Liu, A. H. Kitai, and P. Mascher, J. Lumin. **54**, 35 (1992).
[36]B. X. Lin, Z. X. Fu, and Y. B. Jia, Appl. Phys. Lett. **79**, 943 (2001).
[37]A. F. Kohan, G. Ceder, D. Morgan, and Chris G. Van de Walle, Phys. Rev. B **61**, 15019 (2000).
[38]P. Erhart and K. Albe, Appl. Phys. Lett. **88**, 201918 (2006).
[39]R. Vidya, P. Ravindran, H. Fjellvåg, B. G. Svensson, E. Monakhov, M. Ganchenkova, and R. M. Nieminen, Phys. Rev. B **83**, 045206 (2011).
[40]M. D. McCluskey and S. J. Jokela, J. Appl. Phys. **106**, 071101 (2009).
[41]K. Vanheusden, C. H. Seager, W. L. Warren, D. R. Tallant, J. Caruso, M. J. Hampden-Smith, and T. T. Kodas, J. Lumin. **75**, 11 (1997).
[42]K. Vanheusden, C. H. Seager, W. L. Warren, D. R. Tallant, and J. A. Voigt, Appl. Phys. Lett. **68**, 403 (1996).
[43]Z. Q. Chen, S. Yamamoto, M. Maekawa, A. Kawasuso, X. L. Yuan, and T. Sekiguchi, J. Appl. Phys. **94**, 4807 (2003).
[44]J. Zhong, A. H. Kitai, P. Mascher, and W. Puff, J. Electrochem. Soc. **140**, 3644 (1993).
[45]R. H. Webb, Rep. Prog. Phys. **59**, 427 (1996).

[46]A. B. Djurišić, W. C. H. Choy, V. A. L. Roy, Y. H. Leung, C. Y. Kwong, K. W. Cheah, T. K. G. Rao, W. K. Chan, H. F. Lui, and C. Surya, Adv. Funct. Mater. **14**, 856 (2004).

[47]Z.-M. Liao, H.-Z. Zhang, Y.-B. Zhou, J. Xu, J.-M. Zhang, and D.-P. Yu, Phys. Lett. A **372**, 4505 (2008).

[48]D. Wang and N. Reynolds, ISRN Cond. Mat. Phys. **2012**, 950354 (2012).

[49]K. Kodama and T. Uchino, J. Appl. Phys. **111**, 093525 (2012).

[50]C. Wöll, Prog. Surf. Sci. **82**, 55 (2007).

[51]S. J. Clark, J. Robertson, S. Lany, and A. Zunger, Phys. Rev. B **81**, 115311 (2010).